HINODE, TRACE, SOHO, AND GROUND-BASED OBSERVATIONS OF A QUIESCENT PROMINENCE

P. Heinzel

Astronomical Institute, Academy of Sciences of the Czech Republic, 25165 Ondřejov, Czech Republic; pheinzel@asu.cas.cz

B. Schmieder

Observatoire de Paris, Section Meudon, LESIA, 92195 Meudon Principal Cedex, France

F. Fárník and P. Schwartz

Astronomical Institute, Academy of Sciences of the Czech Republic, 25165 Ondřejov, Czech Republic

N. Labrosse

Department of Physics and Astronomy, University of Glasgow, G128QQ Scotland, UK

P. Kotrč

Astronomical Institute, Academy of Sciences of the Czech Republic, 25165 Ondřejov, Czech Republic

U. Anzer

Max-Planck-Institut für Astrophysik, Karl-Schwarzschild-Strasse 1, 85740 Garching, Germany

G. Molodij

Observatoire de Paris, Section Meudon, LESIA, 92195 Meudon Principal Cedex, France

A. Berlicki

Astronomical Institute of the Wrocław University, Kopernika 11, 51-622 Wrocław, Poland

E. E. DeLuca and L. Golub

Harvard-Smithsonian Center for Astrophysics, 60 Garden Street, Cambridge, MA 02138

T. Watanabe

National Astronomical Observatory of Japan, Mitaka, Tokyo, 181-8588, Japan

and

T. Berger

Lockheed Martin Solar and Astrophysics Laboratory, B/252, 3251 Hanover Street, Palo Alto, CA 94304

ABSTRACT

A quiescent prominence was observed by several instruments on 2007 April 25. The temporal evolution was recorded in Hα by the *Hinode* SOT, in X-rays by the *Hinode* XRT, and in the 195 Å channel by *TRACE*. Moreover, ground-based observatories (GBOs) provided calibrated Hα intensities. Simultaneous extreme-UV (EUV) data were also taken by the *Hinode* EIS and *SOHO* SUMER and CDS instruments. Here we have selected the SOT Hα image taken at 13:19 UT, which nicely shows the prominence fine structure. We compare this image with cotemporaneous ones taken by the XRT and *TRACE* and show the intensity variations along several cuts parallel to the solar limb. EIS spectra were obtained about half an hour later. Dark prominence structure clearly seen in the *TRACE* and EIS 195 Å images is due to the prominence absorption in H I, He I, and He II resonance continua plus the coronal emissivity blocking due to the prominence void (cavity). The void clearly visible in the XRT images is entirely due to X-ray emissivity blocking. We use *TRACE*, EIS, and XRT data to estimate the amount of absorption and blocking. The Hα integrated intensities independently provide us with an estimate of the Hα opacity, which is related to the opacity of resonance continua as follows from the non-LTE radiative-transfer modeling. However, spatial averaging of the Hα and EUV data have quite different natures, which must be taken into account when evaluating the true opacities. We demonstrate this important effect here for the first time. Finally, based on this multiwavelength analysis, we discuss the determination of the column densities and the ionization degree of hydrogen in the prominence.

Subject headings: Sun: prominences — Sun: UV radiation — techniques: spectroscopic

1. INTRODUCTION

Spectral observations of solar prominences reveal different aspects of their physical structure according to the lines and continua that are detected (Heinzel 2007b). The majority of prominence emission lines are formed in cooler parts by scattering of the incident radiation coming from the photosphere, chromosphere, and transition region depending on the line-formation conditions. When observed above the limb, prominences typi-cally appear as bright features against the dark corona. This is the case not only for chromospheric lines such as Hα and other Balmer lines, Ca lines, and others, but also for many transition-region lines formed inside the prominence-corona transition region (PCTR). Analysis of such optical and UV/EUV emission lines and continua, based on detailed non-LTE radiative-transfer modeling, can provide us with diagnostics of prominence thermodynamic parameters and the ionization state of the prominence plasma (Heinzel 2007a).

However, some important prominence parameters can also be deduced in a relatively simpler and more straightforward way, which consists in analysis of the coronal-brightness reduction typically observed at prominence positions. It was shown by Daw et al. (1995 and references therein) that the cool chromospheric material seen above the limb can absorb the X-ray and EUV coronal radiation. For limb prominences this absorption was studied by Daw et al. (1995) and by Kucera et al. (1998), who used the *Solar and Heliospheric Observatory* (*SOHO*) Coronal Diagnostic Spectrometer (CDS) observations of selected coronal lines. This method was then further developed, and one can currently distinguish in the literature two complementary approaches, which we denote the "patrol-type" approach and the "multiwavelength" approach. The first approach, patrol-type studies, uses the simplest possible observations, typically only in one coronal line obtained by patrol-like instruments. The advantage is that instruments such as the *SOHO* EUV Imaging Telescope (EIT) or *Transition Region and Coronal Explorer* (*TRACE*) provide large–field-of-view images and can be used to study many different objects and events, including the eruptive prominences that may be related to coronal mass ejections (CMEs). A great disadvantage of the method is a significant limitation in diagnostics capabilities. For this kind of technique, see, e.g., Golub et al. (1999), Mein et al. (2001), Engvold et al. (2001), or the recent work of Gilbert et al. (2005, 2006) and Kucera & Landi (2008). On the other hand, the multiwavelength approach tries to use as many coronal lines as possible, detected by various space instruments in the UV and EUV (*SOHO*, *TRACE*, and the *Hinode* EUV imaging spectrometer [EIS]), together with the broadband X-rays observed by the *Yohkoh* soft X-ray telescope (SXT) and now by the *Hinode* X-ray telescope (XRT), to disentangle the absorption from the emissivity blocking mechanisms and to derive the hydrogen and helium ionization structure of prominences. The great advantage of such an approach is that it reduces the number of unknown quantities that appear in the respective equations. However, these observations require a substantial coordinated effort and planning, and they are usually made in the context of special campaigns, so that only a very few such data sets are available. Moreover, EUV spectrometers such as the Solar Ultraviolet Measurement of Emitted Radiation (SUMER) and Coronal Diagnostic Spectrometer (CDS) on *SOHO* or the *Hinode* EIS provide slit spectra, and rasters are required for sufficient spatial coverage, taking a rather long time to complete. Using *SOHO* and *Yohkoh* instruments, this type of study was performed by Kucera et al. (1998), Schmieder et al. (1999), and recently Anzer et al. (2007). There are several other similar studies devoted to filaments on the disk (see, e.g., Heinzel et al. 2001; Schmieder et al. 2003; Schwartz et al. 2004).

Two basic mechanisms lead to a coronal brightness reduction at the position of a prominence: absorption and emissivity blocking. The absorption of the coronal line radiation in EUV is due to the photoionization of hydrogen (H, hydrogen Lyman continuum below 912 Å), neutral helium (He I, resonance continuum below 504 Å), and ionized helium (He II, resonance continuum below 228 Å). Theoretical aspects of this mechanism were summarized by Anzer & Heinzel (2005), who also give the model relations to the Hα line opacity. By observing suitably selected lines below 912 Å one can in principle diagnose the column densities of H, He I, and He II. The densities derived in this way can be subsequently used to constrain non-LTE models of hydrogen and helium line and continuum formation (Labrosse & Gouttebroze 2004; Heinzel et al. 2005; Gunár et al. 2007). The second mechanism responsible for lowering the brightness of EUV coronal lines is the "emissivity blocking" first discussed in detail by Heinzel et al. (2003) and extensively applied to a fila-

ment study by Schwartz et al. (2004). This blocking is due to the fact that cool structures (prominences) or low-density structures (cavities and voids) in the corona exhibit much reduced emissivity or lack of it in the EUV lines. Anzer & Heinzel (2005) developed a theoretical formulation of the emissivity blocking due to the presence of cool prominence plasmas. Some aspects of the absorption and blocking were recently considered by Gilbert et al. (2005). In subsequent work Anzer et al. (2007) realized that the limb prominences are transparent in soft X-rays and suggested using this for a determination of the amount of emissivity blocking. Their study was based on *Yohkoh* SXT observations of a coronal cavity in which the prominence was located (and observed by *SOHO* EIT and SUMER).

Based on our previous work and experience, we have suggested using the capabilities of the *Hinode* mission for study of prominence absorption and emissivity blocking mechanisms, which in turn can provide useful diagnostics of the ionization state and column densities of hydrogen and helium. Multiwavelength diagnostics are based on *Hinode* EIS and XRT observations, which are complemented by data from *TRACE*, *SOHO*, and *Hinode* solar optical telescope (SOT) and ground-based Hα observations. To collect such multiwavelength data, we organized coordinated observations among all of these instruments, as part of the HOP004 and JOP 178 (study of filaments and prominences) programs.

In § 2 the observations from space as well as from the ground, obtained during the 2007 April coordinated campaign of *Hinode* and *SOHO* SUMER (running JOP 178), are presented. In § 3, the two mechanisms responsible for lowering the coronal EUV line intensities and soft X-ray brightness (absorption and emissivity blocking) are described, and we show the observed intensity contrasts of 195 Å coronal lines and X-rays. Opacities deduced from EUV contrasts are discussed in § 4, while those corresponding to the Hα line are the subject of § 5. In § 6 we derive the optical thickness of the hydrogen Lyman continuum. In § 7 we discuss our results and make estimates of the hydrogen column densities. In § 8 we summarize our results and propose new multiwavelength observations which would represent a next step in satisfying the complex diagnostic requirements. In this paper we also show for the first time how the spatial averaging of the prominence intensity can affect the determination of opacities, namely, in the case of the coronal line absorption model (see the Appendix).

2. OBSERVATIONS

The observations presented in this paper were obtained during a coordinated campaign of prominence studies involving SOT, XRT, and EIS on *Hinode*, MDI (Michelson Doppler Imager), EIT, SUMER, and CDS on *SOHO*, *TRACE*, and several ground-based observatories. These observations were obtained as part of HOP004 and JOP 178, between 2007 April 23 and 29. This was the first *Hinode*-SUMER observing campaign. HOP004 and JOP 178 are dedicated to the study of prominences and filaments, investigating various aspects of their three-dimensional structure and their magnetic environment from the photosphere to the corona.[1]

2.1. *TRACE and Hinode SOT, XRT, and EIS*

The *Hinode* mission has been operating since 2006 October (Kosugi et al. 2007). The prominence under study was well observed on 2007 April 25 by the *Hinode* SOT instrument, between 13:04 and 13:59 UT in the Hα and Ca II H lines. The 50 cm
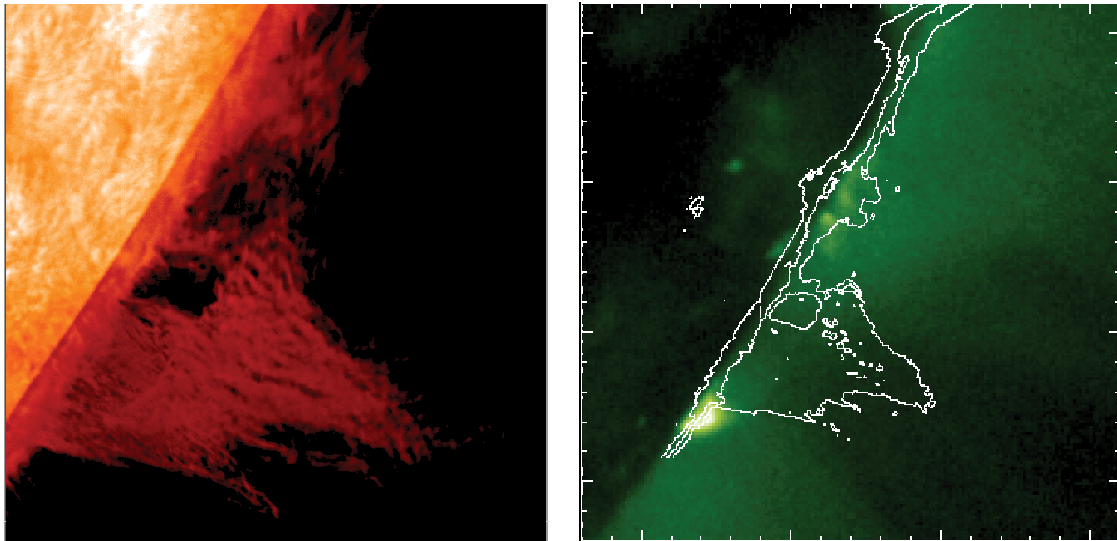
_____

[1] See http://gaia.bagn.obs-mip.fr/jop178/index.html.

Fig. 1.—Hα prominence (*left*) observed on 2007 April 25 at 13:19 UT by *Hinode* SOT (cutoff $80'' \times 80''$) and *Hinode* XRT image (*right*) overlaid by contours of the Hα prominence (20%, 30%, and 40% of the intensity maximum). Each tick is $10''$. A large coronal cavity is seen over the Hα prominence.

aperture telescope can obtain a continuous, seeing-free series of diffraction-limited images in the 3880–6680 Å range with $0.16''$– $0.28''$ spatial resolution (see Suematsu et al. 2008). In our study we use only the Hα images ($160'' \times 160''$) recorded as a 1024×1024 pixel matrix, each pixel having dimensions of $0.16'' \times 0.16''$. The center of the field of view in solar coordinates was $[830'', -510'']$, and the exposure time was 0.3 s. The images are the Level-1 calibrated Hα filtergrams. They have been dark-subtracted, flat-fielded, and corrected for camera readout anomalies. The flat-fielding procedure removes the fringes due to reflections in the CCD chip. The image obtained at time 13:19 UT is shown in Figure 1 (*left*). The field of view of the Ca II H image is smaller ($108'' \times 108''$) and does not cover the entire prominence. Fine structures of the prominence evolve rapidly, especially the round-shaped features at the bottom (Berger et al. 2008). They are rising, and with their quasi-spherical shapes they resemble magnetic separatrices. The material in the prominence lying above these features is very dynamic as they move up. The fine-structure blobs typically move downward. This highly structured and dynamic behavior can be seen in the respective SOT movie, and we plan to discuss it in another paper.

The *Hinode* XRT is a high-resolution grazing-incidence telescope which consists of the X-ray and visible light optics and uses the 2000×2000 pixel CCD camera. A set of filters and a broad range of exposure times enables the telescope to see hot plasmas in the range from 10^5 to 10^8 K. For more details see Golub et al. (2007). Observations of the prominence on 2007 April 25 were done between 13:02 and 13:59 UT with 512×512 pixel coverage, each pixel having size of $1.03'' \times 1.03''$. Filter combination was Al$_{poly}$/Open. The exposure time was 8.19 or 16.38 s, the cadence 60 s.

The *Hinode* EIS is described in detail in Culhane et al. (2007). It observes in two wavelength bands (170–211 and 246–292 Å). Each band has a distinct 1024×2048 pixel CCD detector. The study used in this work is `fil_rast_s2`, which makes a large raster of $240'' \times 256''$ centered on the prominence with the $2''$ slit. At each slit position, a spectrum is obtained with a 50 s exposure. Data from 11 spectral windows are sent back from the satellite: 10 narrow spectral windows (32 pixels wide or 0.714 Å), along with a full spectrum on CCD B of EIS in the wavelength region between 189 and 211 Å. The raster used for this work started at

13:02 UT, and the prominence region was scanned between 13:34 and 13:54 UT. All the relevant data from EIS have been corrected using the software provided by SolarSoft. This includes dark current subtraction, cosmic-ray removal, flat-field correction, and flagging hot pixels, as well as absolute intensity calibration. We also co-aligned the observations obtained through the two detectors. Because of the way the instrument is designed, raster images obtained in the short wavelengths are offset to solar northwest of the long-wavelength images. He II $\lambda256.32$ is used for co-alignment between SOT and EIS, and the heliocentric coordinates stored in the headers of the FITS files thus refer to this line. For these observations, we measure an offset of 1 pixel ($2''$) in the X-direction and 19 pixels ($19''$) in the Y-direction. EIS rasters show a vertical black stripe which unfortunately crosses the prominence. These dark pixels are spectra taken during the night period of the EIS instrument. EIS is an EUV instrument, and the telluric atmosphere at a height of 50 km above sea level absorbs the EUV light from the Sun. In order to remove these dark pixels, we first correct the data at the extreme southern part of the raster image where the corona does not show any feature. We then apply the same correction at all heights. The resulting image is satisfying, and the prominence structure is clearly similar to what is seen on the *TRACE* picture. In addition to the vertical dark stripe there is also a horizontal stripe with an intensity depression (see Fig. 3*b*). This depression is seen only in the intensity integrated over the whole *TRACE* 195 Å bandpass (see Fig. 2), and it is not seen in Fe XII $\lambda195$ alone (compare the dashed and dotted lines in Fig. 7). Due to this fact we assume that this horizontal stripe is caused by some anomaly on the detector. We did not correct data for this stripe because it passes outside the prominence (we instead did not use the data from this part of the raster).

TRACE is a 30 cm aperture Cassegrain normal incidence telescope with a $8.5' \times 8.5'$ field of view and $1''$ spatial resolution. Its CCD detector has 1024×1024 pixels of angular size $0.5''$. For further instrumental details see Handy et al. (1999). Our prominence was observed in the 195 Å bandpass, which enables us to see the plasma with temperature between 0.5 and 2 MK. The prominence was observed between 13:02 and 13:59 UT, the center of the field of view was at the solar coordinates $[799'', -609'']$, and the size of the images during that period is 768×768 pixels ($384'' \times 384''$).
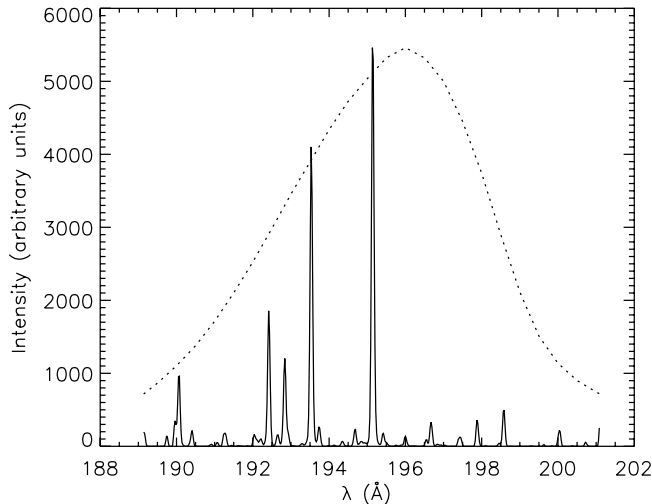
Fig. 2.—EIS spectrum around Fe XII λ195 (*solid line*) and the response function of the *TRACE* 195 Å bandpass (*dotted line*).

2.2. *Co-alignment of Different Observations*

In our analysis we used the SOT Level-1 data in which no correction on instrument misalignment was applied. We defined the SOT Hα image at 13:19 UT as the reference image because all of the instruments were pointing at the prominence at this time (apart from EIS, which was rastering another part of the field of view and detected the prominence region only later). The movies from SOT show an extreme fine-structure activity in the prominence, and thus the overlay should be done for very similar times in order to achieve good accuracy in the measurements. The prominence seen in Hα at this time had a few very well pronounced features, and one of them—a nearly round-shaped dark opening (hole)—was also clearly visible in the *TRACE* 195 Å images as a bright hole within the dark prominence. Therefore, we could use this feature to make an overlay of the *TRACE* image over the Hα one (both taken at the same time) by adjusting the *TRACE* image so that the "openings" precisely overlaid. This enabled us to correct the coordinates of the center of the field of view of the *TRACE* image. Next, we made a new overlay: the XRT image over the *TRACE* one (using its corrected coordinates) so that a few bright disk or near limb features (dots) visible in both images coincided. Again, we could correct the coordinates of the center of the field of view of the XRT image and could overlay the SOT Hα and XRT (Fig. 1). Finally, we had all four data sets (SOT Hα, XRT, EIS, and *TRACE*) in the same coordinate system. This enabled us to make precise comparison between any of the images and, also, to make cuts through the prominence (i.e., to obtain the intensity profiles) along the same lines in all of the data sets (Fig. 3). In order to compare *TRACE* and EIS observations at 195 Å we multiplied the EIS spectrum between 189 and 201 Å (shown in Fig. 2) by the *TRACE* spectral response function (see Fig. 11 in Handy et al. 1998). Note that no continuum emission is detected in the EIS spectrum at these wavelengths (see also N. Labrosse et al. 2008, in preparation).

2.3. *SOHO CDS and SUMER*

The *SOHO* CDS (Harrison et al. 1995) spectrograph observed the prominence between 13:02:45 and 13:31:02 UT. The dimension of the rasters is $244'' \times 240''$. The size of the raster pixel was $4'' \times 3.3''$. Observations were made in seven spectral lines, ordered from lower to higher formation temperature as follows (the

wavelengths in parentheses are given according to CHIANTI database; Dere et al. 1997; Landi & Phillips 2006): He I λ584.33 (584.335 Å), O IV λ554.40 (554.513 Å plus three other, 10 times fainter, O IV lines), O V λ629.15 (629.732 Å), Ca X λ558.48 (557.766 Å), Mg X λ625.04 (624.943 Å), Si XII λ521.27 (520.666 Å), and Fe XIX λ592.77 (592.236 Å). The data were reduced and calibrated in erg cm^{-2} s^{-1} sr^{-1} Å^{-1} using standard SolarSoft procedures for CDS calibration. Along the cuts across the prominence the integrated intensities for each observed line were computed.

The prominence was also observed by the *SOHO* SUMER (Wilhelm et al. 1995) spectrograph in the hydrogen Lyman line series from Lyβ to Lyman continuum. On 2007 April 25, SUMER observed the prominence only after 17:48 UT. This is too far in time from other instrument observations, and therefore, we did not use these data here. However, in a future work we plan to use them for analysis of prominence fine structures (as in Gunár et al. 2007).

2.4. *Ground-based Observations*

Two instruments were used for simultaneous ground-based observations: the imaging Multichannel Subtractive Double Pass (MSDP) spectrograph in Meudon took two-dimensional maps of the Hα line profiles, and the Zeiss's high-dispersion spectrograph with horizontal telescope–HSFA (Horizontal Sonnen-Forschungs Anlage) at Ondřejov Observatory recorded spectra in several lines, including Hα.

With the MSDP spectrograph operating on the Solar Tower of Meudon Observatory, the prominence was observed for three consecutive days, on 2007 April 24, 25, and 26. On April 25 the prominence was observed between 12:09 and 13:32 UT. The entrance slit of the spectrograph covers an elementary field of view of $72'' \times 465''$ with a pixel size of $0.4''$. The final field of view of the images is $500'' \times 465''$. The exposure time was 250 ms. We performed consecutive sequences of 60 images with a cadence of 30 s. The spatial resolution is estimated to be between $1''$ and $2''$, depending on the actual seeing conditions. Using the MSDP technique (Mein 1977, 1991) the Hα image of the field of view is split in wavelength into nine images covering the same field of view. The nine images are recorded simultaneously on a CCD camera. Each image is obtained in a different wavelength interval, and the wavelength separation between images is 0.3 Å. By interpolating with spline functions between the observed intensities in these images, we are able to construct the Hα profile at each point of the observed field of view. A mean or reference disk profile is obtained by averaging over a quiet region on the disk in the vicinity of the prominence (in this case at $\sin \theta = 0.9$). The photometric calibration is done by fitting the reference profile to standard profiles for the quiet Sun (David 1961). We corrected the image for scattered light by analyzing the emission of the nearby corona. The prominence observations in Hα line center by the MSDP spectrograph are well co-aligned with the SOT Hα images obtained at the same time (Fig. 4).

The prominence was also observed with the new multichannel HSFA spectrograph of the Ondřejov Observatory, between 11:17 and 14:00 UT. Four lines, Hα, Hβ, D3, and Ca II K or Ca II H, together with the Hα slit-jaw image, were detected as the prominence was scanned. The diffraction grating enables a spectral resolution of 25 mÅ. The data acquisition system consists of five fast CCD cameras having a 1280×1024 pixel matrix. An exposure time of 150 ms was used for individual spectra. The HSFA diffraction-limit resolution is better than $1''$; however, in these observations it was degraded due to seeing to some $3''$. A standard width of the spectrograph slit for Hα is 100 μm, and the scale of 0.17 mm at

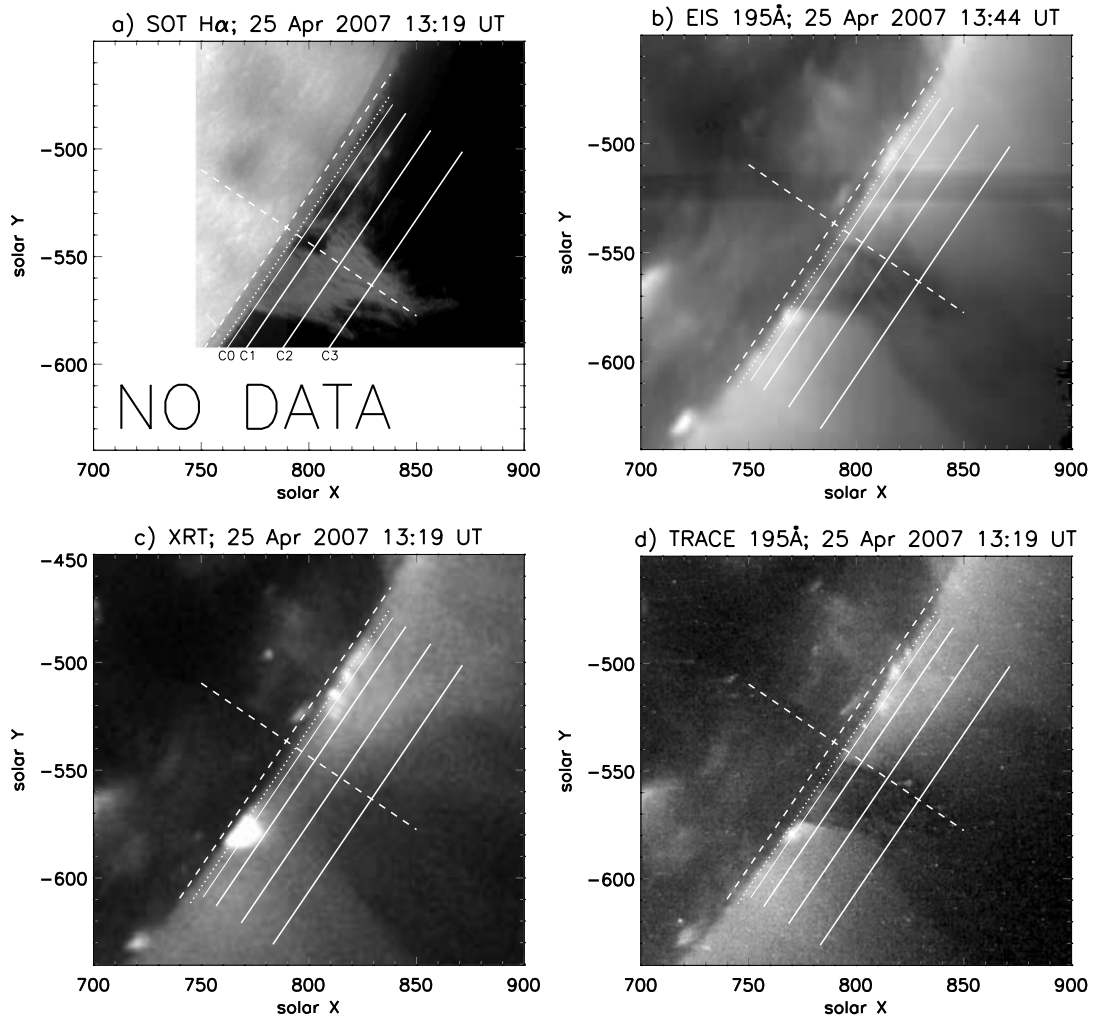Fig. 3.—Multiwavelength images obtained (*a*) with SOT in Hα; (*b*) with EIS in the *TRACE* 195 Å bandpass; (*c*) with XRT; and (*d*) with *TRACE* in the 195 Å bandpass. The cuts numbered 0−3 (*solid white lines*) are overlaid and labeled as C0−C3 in the SOT image in (*a*). Dotted and dashed lines represent the chromospheric and artificial SOT limbs, respectively. The prominence was observed at 13:19 UT by all the instruments except the EIS spectrograph, which rastered it between 13:34 and 13:54 UT. The EIS image is constructed using the response function of the *TRACE* 195 Å bandpass.
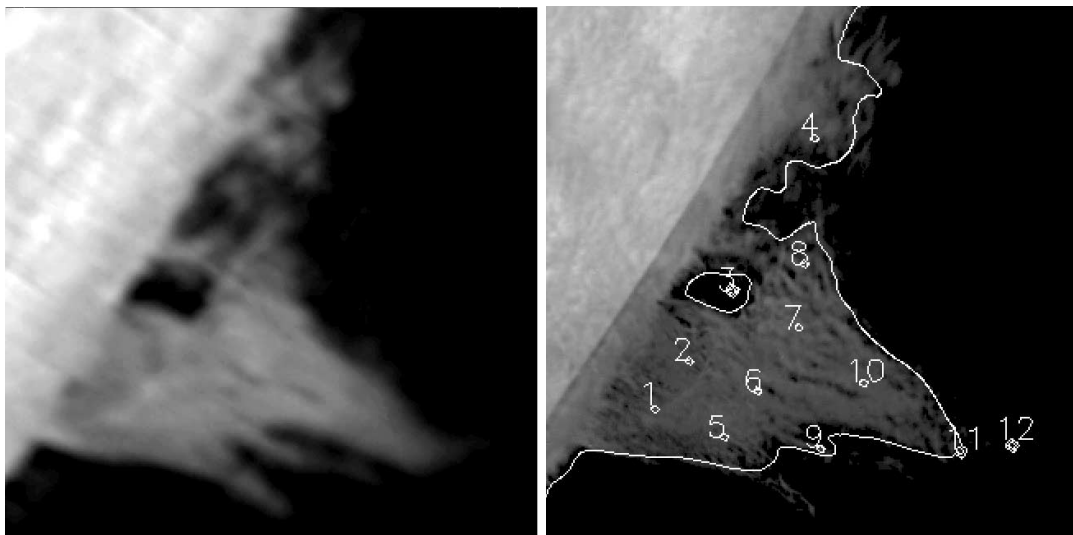

Fig. 4.— Prominence observed in the Hα line center by the MSDP spectrograph (*left*) and by *Hinode* SOT (*right*) on 2007 April 25 at 13:19 UT. On the SOT image we have overlaid the contour of the MSDP observation and indicated points where the opacity has been computed using MSDP and HSFA spectra.
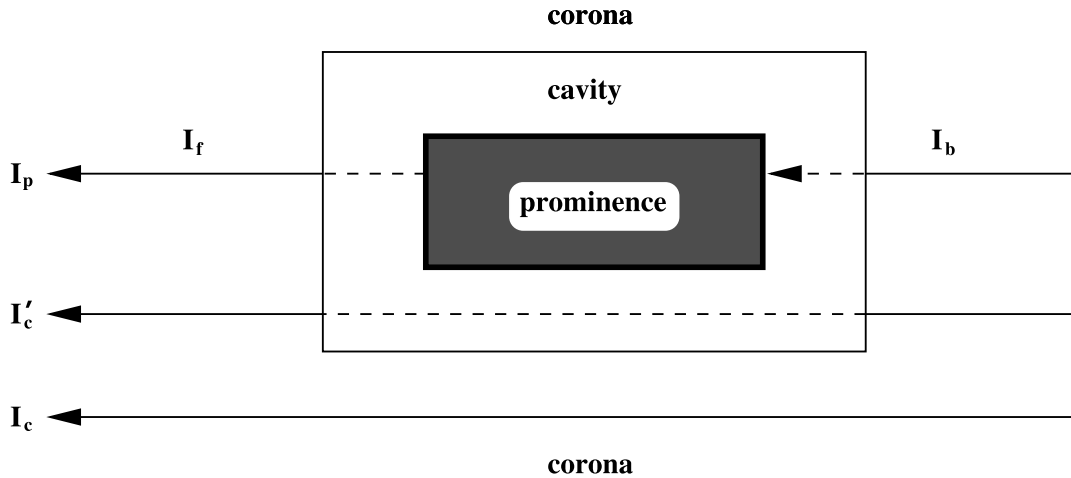
Fig. 5.—Absorption and emissivity blocking scheme, where I_c is the coronal intensity outside the prominence. When the line of sight passes through the cavity surrounding the prominence, I'_c is the intensity of coronal radiation lowered due to the presence of a cavity. In the case of a line of sight passing through the prominence, coronal EUV lines with wavelength below 912 Å are absorbed by the resonance continua of hydrogen and helium in a cool prominence. There is a depression of the coronal brightness due to the cavity plus lack of coronal emission in the prominence volume and the absorption of background radiation I_b. Here I_f is the intensity of radiation emitted by the corona and void in front of the prominence; I_p is the intensity observed at the prominence location. In the XRT observations there is no absorption by the prominence, only a depression of coronal emission due to the cavity plus a lack of coronal emission in the prominence volume. For this case we denoted I_p as I_{cp} in the text and in the equations.

the solar image on the slit corresponds to $1''$. For a description of the HSFA instrument, see Kotrč (2007).

3. ABSORPTION AND EMISSIVITY BLOCKING

3.1. *Mechanisms of Lowering the Coronal Brightness*

Solar prominences observed above the solar limb are usually bright objects seen against a dark coronal background (Fig. 5). This is the case when the spectral observations (rasters or filtergrams) are made in optical lines such as Hα or in transition-region lines. Optical lines are formed in central cool parts of the structure where hydrogen and helium are only partially ionized. Transition-region lines are formed in the prominence-corona transition region (PCTR) at much higher temperatures. Quite a different situation takes place when prominences are observed in coronal lines, i.e., lines of highly ionized metals such as Mg x, Ca x, Si xii, and Fe xii. The prominence itself does not emit radiation in these lines, but the coronal radiation behind the prominence can be strongly absorbed by the hydrogen and helium resonance continua due to the photoionization process. One has to consider the hydrogen Lyman continuum (head at 912 Å), He i continuum (head at 504 Å), and He ii continuum (at 228 Å). The above-mentioned lines detected by CDS are affected only by the hydrogen Lyman continuum, while the *TRACE* 195 Å channel (Fe xi and Fe xii lines) is affected by all three continua. Ideally, using these observations, one could distinguish between hydrogen and helium opacities. A detailed quantitative description of this "absorption mechanism" which leads to a reduction in the coronal brightness at the location of the prominence is presented in Anzer & Heinzel (2005 and references therein).

Using the optical thickness τ_{912} at the hydrogen Lyman continuum head as a reference, we can write for τ at the wavelength position of any EUV coronal lines

$$\frac{\tau}{\tau_{912}} = \frac{\sigma_{\mathrm{H}}}{\sigma_{\mathrm{H}}(912)} + \frac{r_{\mathrm{He}}}{1-i}\left[(1-j_1-j_2)\frac{\sigma_{\mathrm{He\,I}}}{\sigma_{\mathrm{H}}(912)} + j_1\frac{\sigma_{\mathrm{He\,II}}}{\sigma_{\mathrm{H}}(912)}\right],\tag{1}$$

where σ is the photoionization cross section (see Anzer & Heinzel 2005), r_{He} is the helium abundance, which we set to 0.1, i is the

hydrogen ionization degree, and j_1 and j_2 are the neutral and singly ionized helium ionization degrees, respectively. This formula allows us to determine the optical thickness or opacity ratios for any set of these parameters; τ_{912} can be determined from CDS observations or using the theoretical correlation with $\tau_o(\mathrm{H}\alpha)$.

The other mechanism which may lower the coronal brightness in EUV lines is the "emissivity blocking." The coronal emissivity in EUV lines is depressed (or blocked) by the presence of the cool prominence material or low-density cavity (void) around the prominence. This mechanism together with the absorption lowers the coronal brightness (see the cartoon in Fig. 5). If the contrast r is the ratio of the intensity at the prominence position I_p to that outside (in the corona I_c or even within the cavity I'_c), and r_b is the ratio between coronal emission at the same position but at a wavelength where negligible absorption takes place (only blocking), we get (Anzer & Heinzel 2005)

$$r = \frac{1}{2}(1 + e^{-\tau})r_b,\tag{2}$$

and from this we obtain

$$\tau = -\ln\left(2\frac{r}{r_b} - 1\right).\tag{3}$$

This assumes that the coronal line emissivity is symmetrically distributed behind and in front of the prominence (spherically symmetrical corona, with the prominence lying in the plane of the sky).

In Heinzel et al. (2003) and Anzer & Heinzel (2005) the emissivity blocking was introduced to account for an additional reduction of the coronal brightness at the prominence position. Equation (2) properly accounts for the fact that due to the blocking, the coronal background/foreground radiation is lowered compared to the case of a standard quiet corona. The blocking can be due to the prominence itself, to the surrounding void (cavity), or to both. This is schematically drawn in Figure 5. In practice, we can proceed in two equivalent ways in order to account for the blocking effect.

First, we can use equation (2) (or its generalization for an asymmetric corona presented at the end of this subsection) with r

defined as the ratio of the prominence intensity to that in the nearby corona. From the XRT (no absorption) we can determine r_b as the ratio of the coronal intensity at a prominence position to that in the same coronal position for which r was determined. This is based on an assumption that the XRT and the coronal line emission which is absorbed (e.g., 195 Å line) have similar emissivity in the corona, at least in its quiet parts where the lower end of the XRT temperature response overlaps the Fe XII formation temperature; we will check this later using our observational data. However, even for a relatively quiet corona, the solutions obtained from equation (3) will depend somewhat on the actual position in the corona outside the prominence for which r and r_b are computed, simply due to coronal inhomogeneities and noise in the data.

Another equivalent but more efficient way is to again use the assumption of similarity between the XRT and a coronal line emissivity and try to fit their corresponding intensity curves at coronal positions by, e.g., the least-squares method. Then I_c (or I_c') in both r and r_b will be identical, and we can write

$$r = \frac{I_p}{I_c} = \frac{1}{2}(1 + e^{-\tau})\frac{I_{cp}}{I_c}, \qquad (4)$$

from which we simply get

$$r' = \frac{I_p}{I_{cp}} = \frac{1}{2}(1 + e^{-\tau}), \qquad (5)$$

$$\tau = -\ln(2r' - 1). \qquad (6)$$

In our case, I_{cp} represents the XRT intensity *at the position of the prominence*, provided that in the corona *outside the prominence* both the XRT and coronal line intensities are the same (i.e., normalized to each other). In other words, the XRT intensity serves here as a proxy of the coronal line intensity and can be used at positions where the coronal line is normally absorbed by the prominence body. This approach is also very illustrative. The coronal line intensity at the prominence position shows the combined effect of absorption and blocking, while the XRT shows directly the relative amount of blocking (note that this blocking naturally accounts for all kinds of emissivity depression of the coronal line, due to the presence of both the prominence and the cavity). Their ratio at a prominence position then gives the amount of absorption as expressed in equation (5). Note that according to this formula, a minimum value of I_p is $\frac{1}{2}I_{cp}$, in our case $\frac{1}{2}I_{XRT}$. This corresponds to a saturation of the absorption for large τ. For such a case, the solution for τ can still be obtained using an asymmetrical corona. We can write that the background radiation intensity I_b at the prominence position is that derived from the XRT, multiplied by a factor $0 \le \alpha \le 1$. Then the foreground intensity I_f will be the $(1 - \alpha)$ fraction of the XRT intensity. For a symmetrical corona the parameter α is equal to $\frac{1}{2}$. With this we can write a generalized formula

$$r' = \frac{I_p}{I_{cp}} = \alpha(\beta + e^{-\tau}), \qquad (7)$$

where

$$I_p = I_f + I_b e^{-\tau} I_{cp} = I_f + I_b \qquad (8)$$

and $\beta = (1 - \alpha)/\alpha$. For the optical thickness we then get

$$\tau = -\ln\left(\frac{r'}{\alpha} - \beta\right). \qquad (9)$$

A saturation of the absorption for large τ leads to a limiting contrast equal to $1 - \alpha$, which in the case of a symmetric corona gives the value 0.5. However, note that if we replace this true τ by an averaged value related to the spatial filling factor f (see the Appendix), we arrive at a limiting contrast equal to $1 - \alpha f$. This can be important for EUV lines which lie over the hydrogen Lyman continuum (CDS or SUMER lines such as Mg X).

3.2. *A Comparison of Multiwavelength Images—Qualitative Signatures of the Absorption and Blocking*

The multiwavelength images observed at the same time were co-aligned using the pointing coordinates of the header with corrections due to misalignment (see § 2). We chose as a common time 13:19 UT when it is possible or the nearby observations when it is not. The EIS rasters the prominence between 13:34 and 13:54 UT. The multiwavelength images are presented in Figure 3. The EIS image is obtained after applying the response function of the *TRACE* 195 Å passband. In the Hα and CDS transition-region (PCTR) lines (not shown in this paper) we see the prominence in emission above the limb; with *TRACE* and the EIS in 195 Å the prominence is dark. The prominence reaches an altitude of $50''$ (36,000 km) at its top. With the XRT we see a huge bubble over the limb, $100''$ (73,000 km) wide and more than $200''$ long— this is the coronal cavity (void) around the prominence. At XRT wavelengths there is negligible absorption by resonance continua (they are transparent as shown recently by Anzer et al. 2007) so that the prominence is not visible. In this case also the emissivity blocking due to the prominence itself (if the line-of-sight structure were long enough) would cause no significant prominence visibility because the prominence is embedded into an already low-density (low-emissivity) cavity. The prominence that we observed was previously a long quiescent filament, very faint and very wide, lying along a parallel between $30°$ and $35°$ in the southern hemisphere. Due to its length and its position on the disk the cavity could be observed during three consecutive days from 2007 April 24 to 26. This picture is consistent with the geometrical considerations as presented by Fuller et al. (2008).

3.3. *X-Ray and EUV Line Intensity Contrasts*

The construction of the intensity cuts has been done as follows. Heights of the cuts above the solar surface were chosen so that they were passing close to the sets of points denoted 1, 2, 3 (cut No. 1); 5, 6, 7 (cut No. 2); and 9, 10 (cut No. 3; see Fig. 4) where the Hα data from the MSDP and Ondřejov multichannel spectrograph HSFA were reduced. We add a cut No. 0 closer to the limb. The positions of the cuts are shown in Figure 3. In this figure the dashed line indicates an artificial limb of the SOT, which is not the true photospheric limb but which we can use as a reference. The dotted line then marks the bright Hα chromospheric limb. In the EIS and *TRACE* images the chromospheric limb is dark and is also marked by the same dotted line (the reason for this is that the Hα opacity is quite similar to that of resonance continua at 195 Å; this important behavior is discussed later). Finally, we also mark the XRT limb by same dotted line, assuming that it is dark as in the 195 Å line, because of the chromospheric absorption of the background coronal X-ray radiation (Daw et al. 1995).

All four cuts were constructed to be parallel with the tangent to the limb and are $157''$ long (for the mean Sun-Earth distance). Cut 0 was constructed at the height $8.7''$ above the SOT artificial limb (6525 km), cut 1 at the height $16''$ (11,800 km), cut 2 at the height $30''$ (22,100 km), and cut 3 at the height $48''$ (35,300 km). For each instrument, all positions along the cuts were transformed
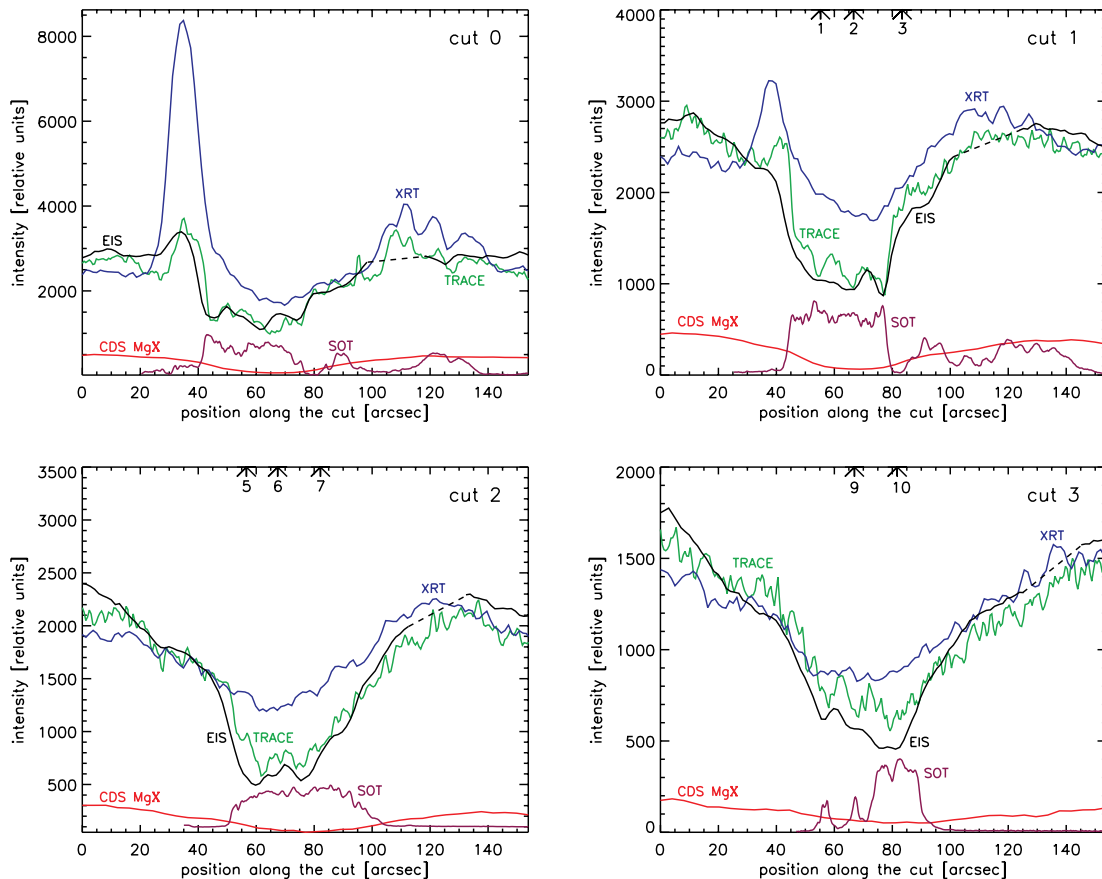
Fig. 6.—Cuts through the prominence at different altitudes over the limb. Positions of the cuts are shown in Fig. 3. Intensities of XRT, EIS 195 Å, *TRACE* 195 Å, and CDS Mg x are in relative units. Intensities of Hα from SOT observations were rescaled and placed at the bottom of the plots. The EIS data plotted with dashed lines mark sections where the cuts cross the horizontal dark stripe. Arrows at the top of the plots mark the positions of the points shown in Fig. 4.

from the solar-disk coordinate system expressed in arcseconds into the image-centered coordinate system expressed in pixels. If the image coordinates of any position along the cut are not integer numbers, then the weighted average of all adjacent pixels (in both the *X*- and *Y*-directions) to that position is taken. Weights were computed as follows: the closer to the exact image position the pixel lies, the higher weight this pixel has in averaging. For the CDS the coordinates in arcseconds need to be transformed from the Sun-*SOHO* distance to Sun-Earth distance, and then the conversion to pixel position can be processed by taking into account the fact that the CDS prominence was rastered between 13:07 and 13:15 UT. Similar corrections have been made for the EIS prominence region that was scanned between 13:34 and 13:54 UT.

To reduce noise the cut regions were constructed using one or two adjacent cuts on each side of each cut for all instrument observations so that they formed a box of similar widths: 2.5″ for XRT, *TRACE*, and EIS and 4.9″ for CDS.

Figure 6 shows the intensity depressions inside the prominence. The intensities of the corona outside the prominence and the cavity have been overlaid in order to derive directly the ratios between the depression and the corona. There is a general agreement between the EIS and *TRACE* cuts.

We examined the influence of spectral integration over the 195 Å bandpass of the *TRACE* instrument on the intensity depression at the prominence. We compared the depressions along all four cuts for three types of data: *TRACE* 195 Å data, intensities from the EIS observations integrated over the spectra in the range of the *TRACE* 195 Å bandpass, also taking into account the re-

sponse function of the *TRACE* 195 Å bandpass, and intensities from the EIS observations integrated over the Fe XII line only. An example of the comparison for cut 1 is shown in Figure 7. We found that the depressions in all three types of the data are very similar for all four cuts; this can be explained by the presence of several other coronal lines (except Fe XII λ195) in the spectrum in
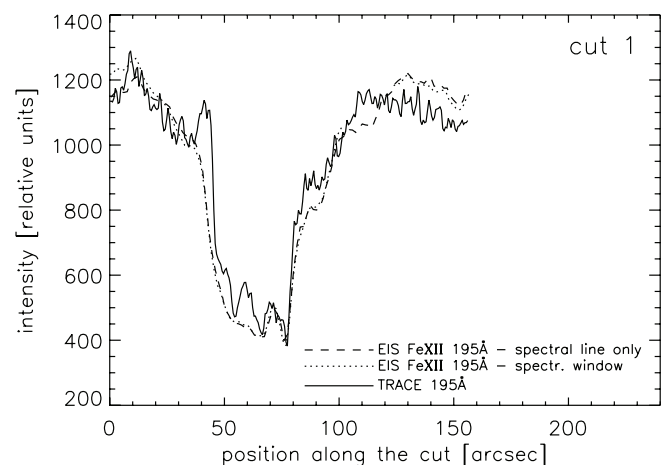

Fig. 7.—Comparison of data from cut 1 observed by EIS in Fe XII λ195 only, by EIS integrated over the *TRACE* 195 Å bandpass, and by *TRACE* in its 195 Å bandpass. Integrated EIS data are interrupted between positions 101″ and 124″ along the cut because the cut crosses the dark horizontal stripe (see Fig. 3b) where data are not reliable.
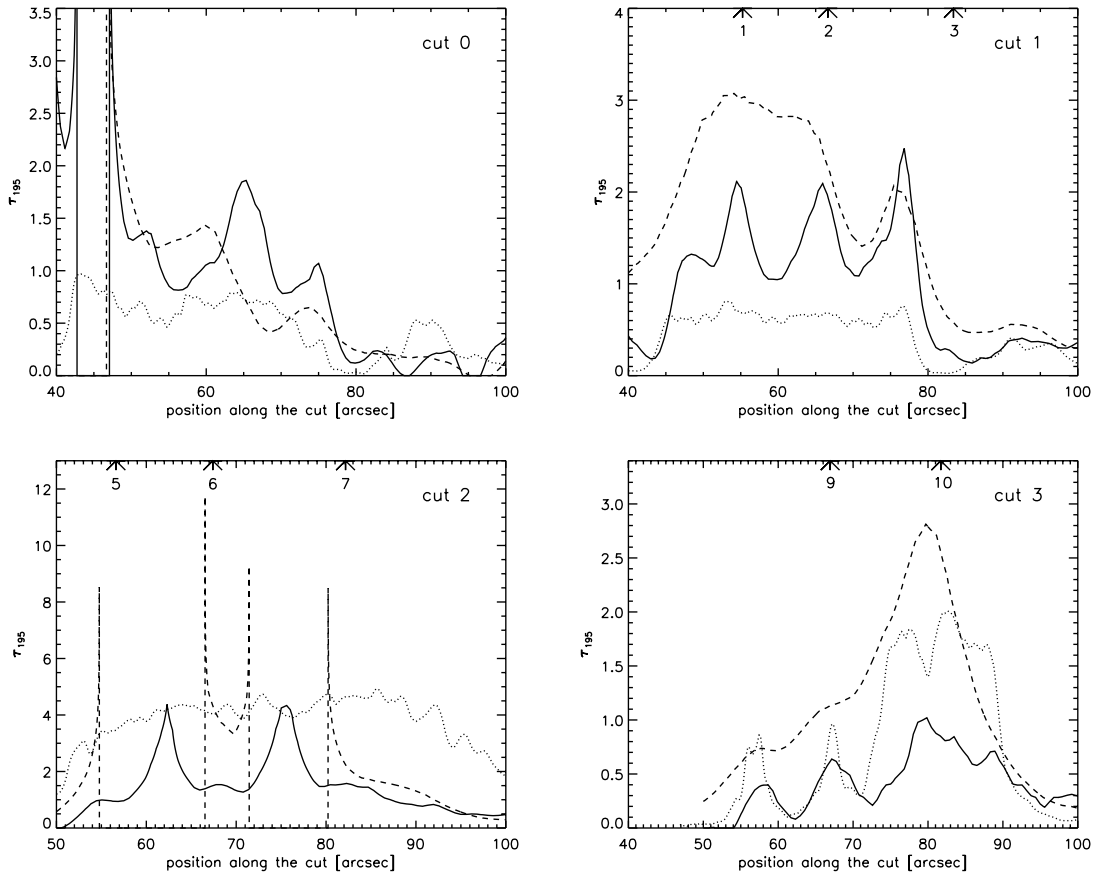
Fig. 8.—Plots of the optical thickness τ_{195} of the resonance continua at 195 Å along the individual cuts computed for $\alpha = 0.5$ from intensity ratios of *TRACE* 195 Å and XRT (*solid lines*) and from ratios of EIS (integrated over the *TRACE* bandpass) and XRT (*dashed lines*). Dotted lines show rescaled and vertically shifted distributions of the Hα emission as observed by SOT. Arrows at the top of the plots mark the positions of points shown in Fig. 4.

the range of the *TRACE* 195 Å bandpass (see Fig. 2) which have the same behavior as the Fe XII line.

4. OPACITIES DEDUCED FROM EUV CONTRASTS

For all four cuts we used the novel procedure to determine τ as described at the end of § 3.1. Along each cut we have selected regions which lie outside the Hα prominence as seen by SOT and which do not contain active brightenings like that on cut 0 at position 35 (Fig. 6). This is considered to be a "quiet" corona for which we believe that the X-ray emissivity is similar to that of Fe XII λ195. We therefore try to fit both the XRT and *TRACE* intensity curves using the least-squares technique. The results are shown in Figure 6, where a reasonably good fit was found for all four cuts, even in regions which correspond to the coronal cavity (see, e.g., cuts 2 and 3 at positions 0–50). On the other hand, bright active regions above the limb (namely, in cut 0) are much brighter in X-rays than in the Fe XII line, which indicates a large temperature difference in the corona. Significantly reduced Fe XII emission at this position is not due to the absorption because there is no cool structure visible in the SOT data. Note that the XRT intensity at the prominence position, compared to that in the external corona, gives the emissivity blocking due to both the prominence and the cavity. On the other hand, *TRACE* and the EIS at the same position show the combined effect of absorption and blocking. The difference between the XRT and *TRACE*/EIS is then entirely due to the absorption; see the plots in Figure 6 at the positions of the SOT Hα emission.

Finally, we have also tried to fit the EIS intensity curves to those of *TRACE* at the same quiet-corona positions. This resulted in

somewhat lower EIS intensities at the prominence positions as compared to *TRACE*. As mentioned above, the integrated EIS spectrum over the *TRACE* 195 Å channel (see Fig. 2) gives almost identical results as for Fe XII λ195 alone, which indicates that both instruments should give the same intensity in this channel. However, *TRACE* is not a spectrograph, the spatial resolution of both instruments is not the same, and, moreover, the EIS data were obtained about half an hour later than the *TRACE* data (the prominence fine structure is evolving in time, and we can check the relative brightness of the SOT Hα at different times). To derive τ at 195 Å, we first used the assumption of a symmetrical corona and computed the optical thickness at all prominence positions using equation (9) with $\alpha = \frac{1}{2}$. The result is shown in Figure 8, for all four cuts. We see that τ at the darkest points of *TRACE* in cut 2 can reach values around 4, while the EIS gives generally larger values, although in the case of cut 2, the EIS data give no solution in many places; i.e., the EIS intensity is lower than $\frac{1}{2}$ that of the XRT. As a next step, we assumed that I_b is larger than I_f, which seems to be consistent with our (rather noisy) data from the CDS in the Mg X line. The hydrogen Lyman continuum at the wavelength position of this line (625 Å) is optically thick in cases when τ_{195} is around 1 or larger. This then means that the absorption of the background coronal radiation in the Mg X line is saturated (see also Kucera et al. 1998 or Schmieder et al. 1999), and we actually see, at the darkest prominence places, only the foreground coronal radiation (provided that the filling factor f is equal to 1; otherwise the limiting contrast is equal to $1 - \alpha f$ as was shown above). From our Mg X cuts we generally see that the intensity at the darkest prominence positions is in several cases lower than
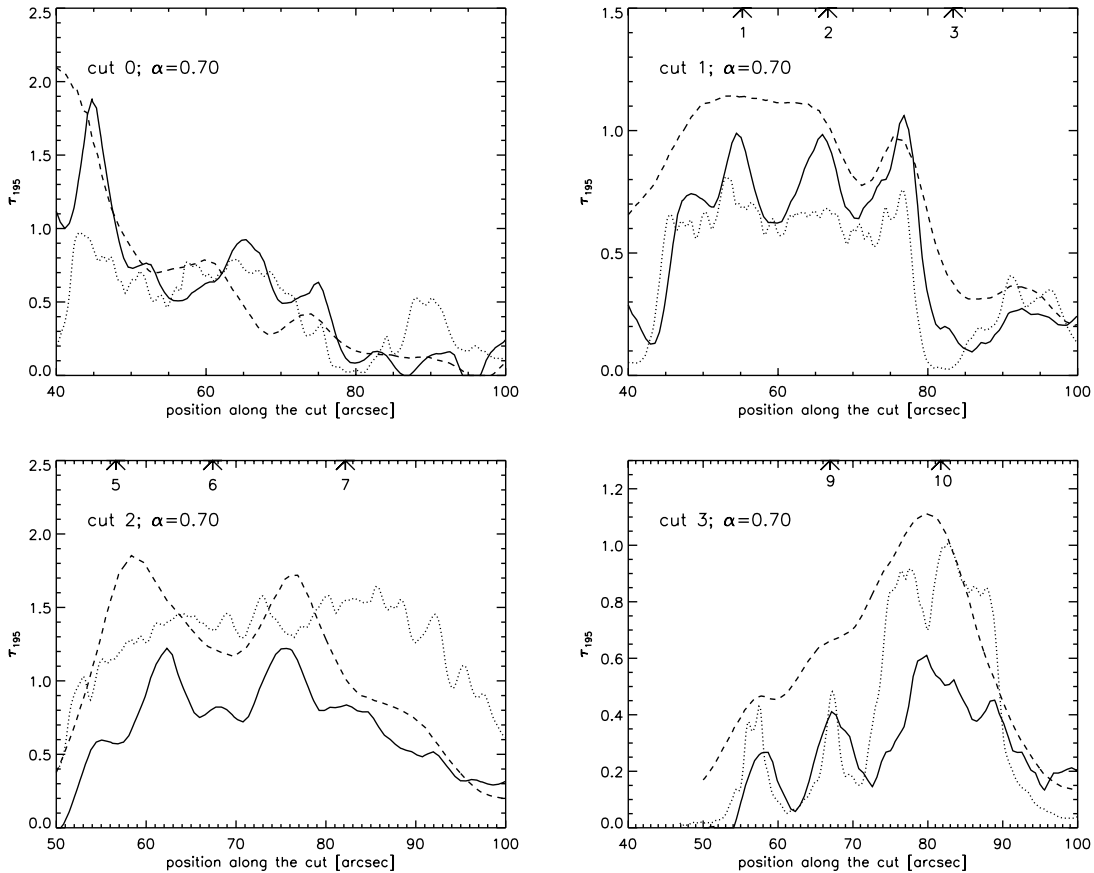
Fig. 9.—Same as Fig. 8, but for $\alpha = 0.7$.

one-half of the fitted XRT intensity. Therefore, we tested our solutions with $\alpha = 0.7$. The results obtained with equation (9) are shown in Figure 9. In this figure all points along cut 2 now have a reasonable solution for the EIS data, and moreover, τ computed for both the EIS and *TRACE* are now naturally lower than for a symmetrical case. As we will see later, this corresponds better to values of $\tau_o(\mathrm{H}\alpha)$ discussed in the next section. We give the values of τ_{195} at selected points detected by MSDP in Table 1.

TABLE 1
VALUES OF τ_{195} AT SELECTED POINTS DETECTED BY MSDP

Point	E(MSDP)	E(HSFA)	Difference (%)	τ_0
1......................	1.11	1.07	4	1.3
2......................	0.98	1.17	16	1.2
3......................	0.23	...	...	0.2
4......................	0.77	...	...	0.8
5......................	0.94	1.27	26	1.1
6......................	1.17	1.36	14	1.4
7......................	1.11	0.94	18	1.3
8......................	0.58	...	...	0.6
9......................	0.47	...	...	0.5
10......................	1.16	1.31	11	1.4
11......................	0.42	...	...	0.4
12......................	0.11	...	...	0.1

NOTES.—Integrated intensities E of the Hα line as determined from MSDP and HSFA observations at the positions indicated in Fig. 4; E is in units 10^5 erg cm^{-2} s^{-1} sr^{-1}. We also indicate the difference between the two observations. The line-center optical thickness was finally derived using the MSDP data.

One distinct feature is the very bright point in cut 0 around position 35, which shows a strong brightening in X-rays. Inspection of the *TRACE* and EIS images indicates a very sharp absorption edge which we interpret as due to the absorption of the radiation from a strong background source, with a negligible foreground contribution. In this case our parameter α may reach unity, and thus the values of τ in Figure 9 computed for $\alpha = 0.7$ might be overestimated at the position of this brightening.

In Figure 6 we can also see a relatively good anticorrelation between *TRACE* intensities and the SOT Hα brightness. For example, in cut 3 we note two narrower minima in the *TRACE* curve (roughly at positions 58 and 68) and one broader minimum around position 80, which correspond to Hα maxima in the SOT curve. This is further reflected in Figures 8 and 9, where τ_{195} correlates quite well with the Hα brightness. However, the correlation of Hα with the EIS intensity curves is less convincing.

5. OPACITY IN THE Hα LINE

5.1. *The Method*

As demonstrated by Heinzel et al. (2001) and later by Anzer & Heinzel (2005), there exists a close correlation between the opacity of the hydrogen Lyman continuum and that of the Hα line. Therefore, the knowledge of the Hα line opacity or the line-center optical thickness of the prominence $\tau_o(\mathrm{H}\alpha)$ immediately gives us an estimate of the Lyman continuum absorption and, using the results of Anzer & Heinzel (2005), also the absorption by helium resonance continua. The thickness $\tau_o(\mathrm{H}\alpha)$ is well correlated with the integrated intensity of Hα as follows from theoretical non-LTE models of Gouttebroze et al. (1993). This correlation is shown in Heinzel et al. (1994, see their Fig. 5), where one can

TABLE 2
Optical Thickness at Selected Points

Point	TRACE	EIS	CDS	Hα
1........................	2.0 (0.95)	3.0 (1.12)	...	1.3
2........................	1.9 (0.95)	2.2 (1.0)	...	1.2
3........................	0.25 (0.17)	0.55 (0.37)	...	0.2
5........................	1.0 (0.58)	(1.65)	0.7	1.1
6........................	1.5 (0.8)	3.5 (1.2)	2.2	1.4
7........................	1.6 (0.83)	2.2 (1.0)	...	1.3
9........................	0.6 (0.4)	1.1 (0.65)	1.1	0.5
10......................	0.85 (0.53)	2.5 (1.08)	1.7	1.4

Notes.—Optical thickness at 195 Å and at Mg x $\lambda 625$ computed from EUV absorption by resonance continua and $\tau_o(H\alpha)$ obtained from the Hα integrated intensity. We give two values for EUV absorption, for symmetrical corona and for $\alpha = 0.7$ (values in parentheses).

see a rather weak dependence on the temperature. To obtain the integrated line intensity, we used both MSDP and HSFA observations. Along the cuts analyzed in the previous section we have selected several points in which the Hα line intensity was determined; see Figure 4, where these points are marked within the SOT image taken almost at the same time.

5.2. Calibration of Hα Ground-based Observations

The normalization of the intensities of the MSDP was done as follows. The intensities of the observed profiles I_λ are automatically normalized to the local continuum $I_\lambda/(I_{c,\mathrm{loc}})_{\mathrm{obs}}$. In order to compare the observed intensities with those calculated theoretically, we renormalize the intensities to the continuum at disk center I_λ/I_c. The continuum at disk center in the wavelength region close to the Hα line has intensity $I_c = 4.077 \times 10^{-5}$ erg cm^{-2} s^{-1} sr^{-1} Hz^{-1}. To renormalize we must apply two corrections: (1) One is due to the limb darkening. The reference profiles are measured on the disk near the limb at $\sin\theta = 0.98$. It reduced the intensity by a factor of 0.547. (2) The central intensity is no longer equal to 16% of the intensity of the continuum but is equal to 22.6%.

The normalization of the intensities of the HSFA was done as follows. The Hα spectra were corrected for dark frames and flat-fielded in a standard way. Then the dispersion relation was found by comparing the positions of about 20 spectral lines in the field of view of the spectral strip close to the Hα line with those in the solar spectral atlas. Relative intensity profiles of the solar limb were compared to the corresponding Hα intensity profiles of David (1961) to find a factor converting them into local continuum values. Then using relations of Allen (1985) for the center-limb darkening, the conversion to intensity units expressed in erg s^{-1} cm^{-2} sr^{-1} Å^{-1} was carried out. Scattered light was subtracted, and the Hα line profiles in selected places of the prominence were integrated to obtain the integrated intensities.

5.3. Results

In Table 1 we present the Hα integrated intensities at points marked in Figure 4 (note that the HSFA data calibration was not performed at all these points but only in the brightest ones). We see that the results from both GBOs are quite compatible, the differences being typically less than 20% (due to calibration, scattered light, instrumental differences, etc.). These intensities can be directly used to obtain the values of $\tau_o(H\alpha)$, i.e., the line-center optical thickness of the prominence along the line of sight, at selected points. As already mentioned, the temperature dependence is rather weak, and here we used $T = 8000$ K as a typical

TABLE 3
Theoretical Optical Thicknesses and Hydrogen Ionization Degree i According to Anzer & Heinzel (2005)

$\tau_o(H\alpha)$	T (K)	τ_{195}	τ_{912}	i
0.5.............................	6000	0.9	13	0.66
	8000	1.0	13	0.70
1.0.............................	6000	1.7	30	0.56
	8000	1.6	25	0.62
2.0.............................	6000	3.2	70	0.43
	8000	2.8	50	0.56

temperature of the Hα forming regions. The resulting $\tau_o(H\alpha)$ is given in Table 1.

6. OPTICAL THICKNESS OF THE HYDROGEN LYMAN CONTINUUM

Using TRACE, EIS, CDS, and Hα data we are able to derive τ_{912}.

6.1. TRACE, EIS, and XRT

The optical thickness at 195 Å was obtained in § 3. To convert this τ to that at the head of the hydrogen Lyman continuum, we use the approximate relation of Anzer & Heinzel (2005),

$$\tau_{195}/\tau_{912} \simeq 12.09 \times 10^{-3} + 1.93 \times 10^{-2} f(i), \qquad (10)$$

where $f(i) = 1/(1 - i)$ depends on the mean hydrogen ionization degree $i = N_p/N_H$ with N_p and N_H being, respectively, the proton and total hydrogen column density. Note that this equation was derived assuming a relative helium abundance $r_{He} = 0.1$ and a negligible population of the He III state (which seems to be reasonable inside the cool parts of the absorbing prominence medium). The great advantage of this formula is that it does not depend on He II population—this follows from a rough equality between He I and He II continuum opacity at 195 Å (Mein et al. 2001; Anzer & Heinzel 2005). If He III has nonnegligible abundance in the cool parts of a prominence, the function $f(i)$ in equation (10) is replaced by $f(i, j_2) = (1 - j_2)/(1 - i)$. Nonzero j_2 clearly lowers the opacity at 195 Å, and the corresponding τ becomes comparable to $\tau_o(H\alpha)$.

6.2. CDS and XRT

The most reliable coronal CDS data obtained for this prominence are those for Mg x $\lambda 625$, where the signal-to-noise ratio is at a reasonable level. Ca x and Si XII data are much noisier. At the wavelength position of the Mg x line, the optical thickness of the hydrogen Lyman continuum (only this continuum matters) is computed using equation (3), which takes into account the emissivity blocking contrast derived from the XRT images. The computed optical thickness at selected points marked in Figure 4 is given in Table 2. However, these values of τ are too low and inconsistent with the TRACE and EIS results. We can compare $\tau_{912} = 2.5\tau_{625}$ with τ_{912} given in Table 3 for values of $\tau_o(H\alpha)$ and τ_{195} derived from our optical and TRACE data. The difference is large, in most cases reaching almost 1 order of magnitude. Therefore, the CDS data cannot be used to derive τ_{912} directly, although this method would be the most straightforward. The following aspects of the problem are worth discussing. For large τ_{912}, which follow from optical and TRACE/EIS data, the absorption of Mg x would be saturated—such saturation is frequently met in the data, as noted by Kucera et al. (1998) and Schmieder et al. (1999). However, in

cases where the prominence is less optically thick in the 195 Å channel, the Mg x line can be used to derive reliable values of τ_{912} provided that this line is observed with a favorable signal-to-noise ratio (see the results from *SOHO* SUMER observations presented by Anzer et al. 2007).

7. DISCUSSION OF RESULTS

We see from Table 2 that $\tau_o(H\alpha)$ obtained from GBO data is quite similar to τ_{195}. This result was already obtained in Mein et al. (2001) and Schmieder et al. (2004) using *TRACE* and $H\alpha$ data for, respectively, an arch filament system and a filament, where a similar fine structure was seen at both wavelengths. The theoretical grounds of this important correlation were discussed by Anzer & Heinzel (2005) and are shown in Table 3. However, in our present observations these values are not consistent with the optical thickness of the hydrogen Lyman continuum derived here from CDS lines. Considering the Mg x line (other lines are more noisy), we have $\tau_{912} = 2.5\tau_{625}$. This gives values of τ_{912} which are much lower than the theoretical values shown in Table 3. A similar or even worse situation arises for Ca x and Si xII lines at points 1 and 2.

7.1. *Spatial Averaging of Optical and EUV Intensities*

Assuming that the CDS data are accurate enough and have been correctly reduced/calibrated, the only explanation we can suggest here is the influence of a spatial averaging. This explanation is possible thanks to information from high-resolution images taken by the SOT. Although we could not use SOT images directly to obtain $\tau_o(H\alpha)$ (only the line-center intensity was detected, and this was not radiometrically calibrated), we see from them that at spatial resolution $0.2''$–$0.3''$, *TRACE*, CDS, and GBO $H\alpha$ contain many fine-structure elements within the spatial box over which the intensities have been averaged. Actually *TRACE* has a spatial resolution around $1''$ and the CDS around $4''$, and the GBO $H\alpha$ spatial resolution is also several arcseconds because of the seeing; moreover, we have integrated over several pixels to obtain our cuts. In the Appendix we demonstrate that in the case of EUV absorption, the mean τ is related to the τ of individual fine structures in a *nonlinear* way, while for $H\alpha$ this relation is linear. As follows from Figure 10, the low values of τ obtained from CDS lines can be related to a specific value of the filling factor. The saturation of curves which correspond to nonlinear averaging demonstrates that by increasing the true τ, the mean τ can only reach the value $-\ln(1-f)$ (in the case of a symmetric corona and under the assumptions used in the Appendix). Taking the mean value of the derived τ_{625} from Table 3, which is about 1.6, we see that this is the saturated value for $f = 0.8$. Note that this value of f together with $\alpha = 0.7$ assumed above for the case of a nonsymmetric corona leads to a limiting contrast in the Mg x line equal to $1 - \alpha f = 0.44$, which still indicates a saturation (lowering f requires larger values of α).

The effect of low spatial resolution due to seeing is much less critical for the $H\alpha$ line as we can also see from Figure 10, where the averaged τ is related to the true one by straight dashed lines. In addition, τ_{195} is not affected as much by the spatial resolution and data averaging of *TRACE*, first because *TRACE* has better resolution than the CDS, and second because τ_{195} is around 1 and thus the nonlinear averaging is not saturated. We see that for all values of a given f, the true τ_{195} is always larger than $\tau_o(H\alpha)$, provided that the mean values are comparable as in our data. This is consistent with the theoretical results shown in Table 3, where the results for two temperatures are similar. Our values of $\tau_o(H\alpha)$ between 1 and 2 are consistent with a hydrogen ionization degree i
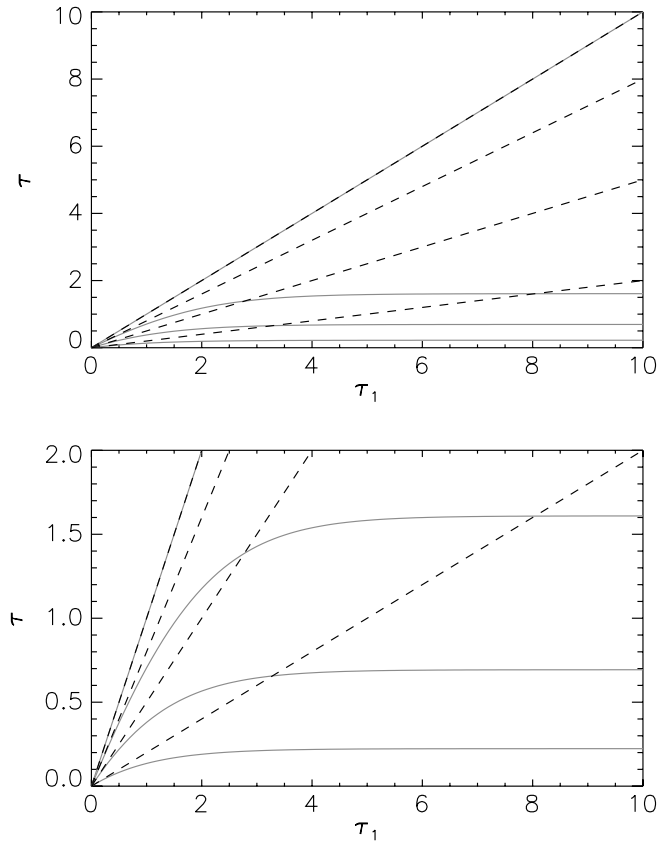

Fig. 10.— Behavior of the two types of spatial averaging, for various values of the filling factor, where τ_1 is the actual optical thickness of the resonance continua at the wavelength position of EUV line under consideration, and τ is the averaged thickness. Solid lines correspond to the EUV case, dashed ones to $H\alpha$. Four curves correspond to four filling factors: 1.0, 0.8, 0.5, and 0.2. The lower plot shows a zoom.

between 0.4 and 0.6. This involves the central cool parts of the prominence, emitting in the $H\alpha$ line and absorbing coronal radiation in EUV resonance continua of hydrogen and helium. Our results also indicate that the ionization degree of singly ionized helium j_2 is small (for our analysis we assumed $j_2 = 0$). This is consistent with the results of non-LTE prominence modeling of Labrosse & Gouttebroze (2004), who also found a negligible abundance of He III in central parts of the prominence slab.

7.2. *Hydrogen Column Density*

Using τ_{195} obtained from our observations, one can directly estimate the hydrogen column density N_H at a given prominence position. Assuming again that the He I and He II continuum cross sections are the same, we get from equation (1)

$$N_H = \frac{\tau_{195}}{(1-i)\sigma_H^{195} + r_{He}\sigma_{He}^{195}}, \qquad (11)$$

and using the data from Anzer & Heinzel (2005) we obtain

$$N_H = \frac{10^{19}}{2 - 0.8i}\tau_{195}, \qquad (12)$$

which for $i = 0.5$ gives simply $N_H = 1.6 \times 10^{19}\tau_{195}$. With the values of τ_{195} shown in Figure 8 we find that N_H is roughly in the range $(1-5) \times 10^{19}$ cm^{-2}. These hydrogen column densities are quite reasonable, comparable to previous results, such as those obtained by Gilbert et al. (2005, 2006) or Anzer et al. (2007). For

a hydrogen density of the order of 10^{11} cm^{-3}, which is characteristic of quiescent prominences at temperatures 6000–8000 K, we get an effective prominence thickness around $(1-5) \times 10^3$ km, which is a quite reasonable value. A great advantage of this method is that the dominant opacity of helium resonance continua does not depend on the ratio He II/He I (j_1 in our notation) but only on total helium density (assuming that the He III density is negligible in cool parts of a prominence; see the non-LTE computations of Labrosse & Gouttebroze 2004). Our solutions thus only assume a knowledge of the hydrogen ionization degree i, but this varies, for a given temperature, within a rather narrow range of values around 0.5 (see Table 3). Note that Gilbert et al. (2005) used a different source of opacity data for He I from which the He I continuum opacity is a factor of 1.5 larger than that of He II (their He II opacity is the same as ours since it simply follows from the hydrogen-like atomic model). This difference, larger than in our case, led the authors not to assume the equality of both opacities, and this, in turn, requires knowledge of j_1. Using the VAL model of the chromosphere (Vernazza et al. 1981), Gilbert et al. (2005) assumed $0.005 \leq j_1 \leq 0.14$, generally lower than values given by Labrosse & Gouttebroze (2004).

8. CONCLUSIONS

In this paper we have used the opportunity to combine multiwavelength prominence data for a detailed quantitative analysis of the EUV coronal line absorption and blocking. We were fortunate to observe a prominence which shows all of the major aspects of these mechanisms, such as the coronal darkening at the prominence position and the cavity around the prominence. A coordinated *Hinode*-SUMER campaign allowed us to obtain the multiwavelength data from several space instruments and GBOs. The *Hinode* XRT allows us to determine the blocking much better than with the *Yohkoh* SXT (used in Anzer et al. 2007), and we have suggested here a modified method which directly uses the XRT intensity curve to account for the emissivity blocking. This study presents the first simultaneous observations in the 195 Å line (channel) by the *Hinode* EIS and *TRACE* with Hα. They confirm, for the prominence situation, that the helium resonance continua opacity is similar at 195 Å and in Hα, a result previously obtained theoretically by Anzer & Heinzel (2005) and observationally for filaments in Schmieder et al. (2004). This result was then used in the analysis of the Hα filament and its channel by Dudík et al. (2008). These opacities are now shown to be consistent with theoretical non-LTE models of prominences, namely, the computation of the Hα and hydrogen Lyman continuum optical thickness. The 195 Å opacities empirically derived here can serve as constraints for non-LTE models of He line and continua formation (Labrosse & Gouttebroze 2004).

Opacity in the hydrogen Lyman continuum could not, however, be determined properly using the Mg x line observed by the CDS. This is probably because of the low spatial resolution of the CDS. We demonstrate here for the first time the importance of high spatial resolution for correct determination of EUV opacities using the absorption/blocking model for prominences. The basic idea of a nonlinear averaging is developed in the Appendix.

The importance of this effect depends on the filling factor, which corresponds to the respective EUV data, and also on the continuum opacity, which is wavelength-dependent.

Our results obtained with *TRACE* seem to be more consistent with Hα observations than are the data from the EIS. The EIS, as the next-generation EUV spectrometer, is supposed to provide excellent data, and thus we think that the problem with our observations is mainly due to the unfortunate circumstance that the *Hinode* satellite passed into an eclipse period exactly at time of the prominence rastering. The way we have corrected the EIS data for this effect may not be optimal, although some of our tests do indicate that no significant error was introduced. Another reason could be the time difference between our *TRACE* and EIS observations—from the SOT prominence movie we clearly see a significant temporal evolution of the prominence fine structure.

Another significant result is the determination of the hydrogen column density, found to be in the range $(1-5) \times 10^{19}$ cm^{-2}, fully consistent with other studies. The technique for determination of prominence column masses based on the analysis of coronal line depressions is promising for studies of prominence eruptions and mass loading of related CMEs (Gilbert et al. 2006).

In conclusion, we suggest performing future multiwavelength observations using more coronal lines by the EIS (including those above 228 Å), calibrated Hα intensities from the SOT, and the XRT, which has proven to provide a useful proxy of coronal line intensities at the place of an absorbing prominence. Moreover, one can also consider simultaneous SUMER observations in selected coronal lines below as well as above 912 Å as discussed in Anzer et al. (2007). We will further develop our non-LTE prominence models to be consistent with the opacities and column densities empirically derived from these multiwavelength prominence observations.

APPENDIX

Let us assume that the SOT spatial resolution is about 0.3$''$, while the intensities measured with EUV space instruments (*TRACE*, *Hinode* EIS, and *SOHO* CDS) are averaged over much larger boxes. If the fine-structure elements have a typical size comparable to the SOT resolution (see part of the SOT image with fine structures in Fig. 1), we will have a large number of them within the resolution box of the EUV space instruments; this can be characterized by a spatial filling factor f. Let us further assume, for simplicity reasons, that

only two different intensities are present for such elements, I_1 and I_2, which correspond to f and $(1-f)$ filling factors, respectively. For the EUV absorption model we then write

$$I_1 = \frac{1}{2}(1 + e^{-\tau_1})I_{cp}, \quad I_2 = \frac{1}{2}(1 + e^{-\tau_2})I_{cp}. \tag{A1}$$

Spatially averaged intensity will be equal to

$$I = fI_1 + (1-f)I_2, \tag{A2}$$

and in terms of averaged τ,

$$I = \frac{1}{2}(1 + e^{-\tau})I_{cp}. \tag{A3}$$

By combining these equations we obtain for mean τ

$$\tau = -\ln[fe^{-\tau_1} + (1-f)e^{-\tau_2}]. \tag{A4}$$

This averaging of τ using the EUV intensities is *nonlinear* due to the absorption terms $e^{-\tau}$. The same formula applies for a non-symmetrical corona, i.e., the averaging does not depend on the parameter α.

Hα intensities as measured by MSDP or HSFA are also averaged over a substantially large box (mainly due to the seeing effect), but in this case the averaging of τ is *linear*, by nature quite different from that for EUV. In case of Hα, the intensity is converted to τ using the linear relation $\log I - \log I_0 = \gamma \log \tau$ (see Heinzel et al. 1994), which simply gives $I = I_0 \tau^\gamma$. With this and with equation (A2) we get

$$\tau = \left[f\tau_1^\gamma + (1-f)\tau_2^\gamma \right]^{1/\gamma}. \tag{A5}$$

Finally, assuming the simplest case when we have a fraction f of fine-structure elements with intensity I_1 and $(1-f)$ of coronal features between them (which have $\tau_2 = 0$), we get for the EUV case

$$\tau = -\ln[fe^{-\tau_1} + (1-f)], \tag{A6}$$

while for Hα we have (taking $\gamma = 1$)

$$\tau = f\tau_1. \tag{A7}$$

Note that for Hα line center τ larger than 1, the parameter γ starts to deviate from unity (e.g., Heinzel et al. 1994).

In Figure 10 we show the behavior of these two types of spatial averaging, for various values of the filling factor. It is important to realize that since the averaged optical thickness depends on the actual τ_1 of the hydrogen and helium EUV continua (i.e., the optical thickness of the hydrogen and helium resonance continua at the wavelength of the measured EUV line), the behavior of the nonlinear averaging is wavelength-dependent. For EUV lines which are absorbed at larger τ_1 (closer to the continuum head) the averaging effect will be more important.

REFERENCES

Allen, E. W. 1985, Astrophysical Quantities (3rd ed.; London: Athlone)
Anzer, U., & Heinzel, P. 2005, ApJ, 622, 714
Anzer, U., Heinzel, P., & Fárnik, F. 2007, Sol. Phys., 242, 43
Berger, T. E., et al. 2008, ApJ, 676, L89
Culhane, J. L., et al. 2007, Sol. Phys., 243, 19
David, K.-H. 1961, Z. Astrophys., 53, 37
Daw, A., Deluca, E. E., & Golub, L. 1995, ApJ, 453, 929
Dere, K. P., Landi, E., Mason, H. E., Monsignori Fossi, B. C., & Young, P. R. 1997, A&AS, 125, 149
Dudík, J., Aulanier, G., Schmieder, B., Bommier, V., & Roudier, T. 2008, Sol. Phys., 248, 29
Engvold, O., Jakobsson, H., Tandberg-Hanssen, E., Gurman, J. B., & Moses, D. 2001, Sol. Phys., 202, 293
Fuller, J., Gibson, S. E., de Toma, G., & Fan, Y. 2008, ApJ, 678, 515
Gilbert, H. R., Falco, L. E., Holzer, T. E., & MacQueen, R. M. 2006, ApJ, 641, 606
Gilbert, H. R., Holzer, T. E., & MacQueen, R. M. 2005, ApJ, 618, 524
Golub, L., et al. 1999, Phys. Plasmas, 6, 2205
———. 2007, Sol. Phys., 243, 63
Gouttebroze, P., Heinzel, P., & Vial, J. C. 1993, A&AS, 99, 513
Gunár, S., Heinzel, P., Schmieder, B., Schwartz, P., & Anzer, U. 2007, A&A, 472, 929
Handy, B. N., Bruner, M. E., Tarbell, T. D., Title, A. M., Wolfson, C. J., Laforge, M. J., & Oliver, J. J. 1998, Sol. Phys., 183, 29
Handy, B. N., et al. 1999, Sol. Phys., 187, 229
Harrison, R. A., et al. 1995, Sol. Phys., 162, 233
Heinzel, P. 2007a, in ASP Conf. Ser. 368, The Physics of Chromospheric Plasmas, ed. P. Heinzel, I. Dorotovič, & R. J. Rutten (San Francisco: ASP), 271

Heinzel, P. 2007b, in ASP Conf. Ser. 370, Solar and Stellar Physics through Eclipses, ed. O. Demircan, S. O. Selam, & B. Albayrak (San Francisco: ASP), 46
Heinzel, P., Anzer, U., & Gunár, S. 2005, A&A, 442, 331
Heinzel, P., Anzer, U., & Schmieder, B. 2003, Sol. Phys., 216, 159
Heinzel, P., Gouttebroze, P., & Vial, J.-C. 1994, A&A, 292, 656
Heinzel, P., Schmieder, B., & Tziotziou, K. 2001, ApJ, 561, L223
Kosugi, T., et al. 2007, Sol. Phys., 243, 3
Kotrč, P. 2007, in ASP Conf. Ser. 368, The Physics of Chromospheric Plasmas, ed. P. Heinzel, I. Dorotovič, & R. J. Rutten (San Francisco: ASP), 559
Kucera, T. A., Andretta, V., & Poland, A. I. 1998, Sol. Phys., 183, 107
Kucera, T. A., & Landi, E. 2008, ApJ, 673, 611
Labrosse, N., & Gouttebroze, P. 2004, ApJ, 617, 614
Landi, E., & Phillips, K. J. H. 2006, ApJS, 166, 421
Mein, N., Schmieder, B., DeLuca, E. E., Heinzel, P., Mein, P., Malherbe, J. M., & Staiger, J. 2001, ApJ, 556, 438
Mein, P. 1977, Sol. Phys., 54, 45
———. 1991, A&A, 248, 669
Schmieder, B., Kotrč, P., Heinzel, P., Kucera, T., & Andretta, V. 1999, in Magnetic Fields and Solar Processes, ed. A. Wilson (ESA SP-448; Noordwijk: ESA), 439
Schmieder, B., Lin, Y., Heinzel, P., & Schwartz, P. 2004, Sol. Phys., 221, 297
Schmieder, B., Tziotziou, K., & Heinzel, P. 2003, A&A, 401, 361
Schwartz, P., Heinzel, P., Anzer, U., & Schmieder, B. 2004, A&A, 421, 323
Suematsu, Y., et al. 2008, Sol. Phys., 249, 197
Vernazza, J. E., Avrett, E. H., & Loeser, R. 1981, ApJS, 45, 635
Wilhelm, K., et al. 1995, Sol. Phys., 162, 189